Physics of Fluids

Pressure distribution and flow dynamics in a nasal airway using a scale resolving simulation

Cite as: Phys. Fluids **33**, 011907 (2021); https://doi.org/10.1063/5.0036095
Submitted: 03 November 2020 . Accepted: 17 December 2020 . Published Online: 29 January 2021

James Van Strien, Kendra Shrestha, Sargon Gabriel, Petros Lappas, David F. Fletcher, Narinder Singh, and Kiao Inthavong

COLLECTIONS

This paper was selected as Featured

This paper was selected as Scilight

View Online Export Citation CrossMark

ARTICLES YOU MAY BE INTERESTED IN

Do you smell what I smell? How nasal geometry affects airflow dynamics
Scilight **2021**, 061103 (2021); https://doi.org/10.1063/10.0003538

On airborne virus transmission in elevators and confined spaces
Physics of Fluids **33**, 011905 (2021); https://doi.org/10.1063/5.0038180

The perspective of fluid flow behavior of respiratory droplets and aerosols through the facemasks in context of SARS-CoV-2
Physics of Fluids **32**, 111301 (2020); https://doi.org/10.1063/5.0029767

© 2021 Author(s).

Physics of Fluids ARTICLE scitation.org/journal/phf

Pressure distribution and flow dynamics in a nasal airway using a scale resolving simulation

Cite as: Phys. Fluids 33, 011907 (2021); doi: 10.1063/5.0036095
Submitted: 3 November 2020 • Accepted: 17 December 2020 •
Published Online: 29 January 2021

View Online Export Citation CrossMark

James Van Strien,[1] Kendra Shrestha,[1] Sargon Gabriel,[2] Petros Lappas,[1] David F. Fletcher,[3] Narinder Singh,[4,a)] and Kiao Inthavong[5,b)]

AFFILIATIONS

[1]Mechanical and Automotive Engineering, School of Engineering, RMIT University, P.O. Box 71, Bundoora 3083, Australia
[2]Manufacturing, Materials and Mechatronics Engineering, School of Engineering, RMIT University, P.O. Box 71, Bundoora 3083, Australia
[3]School of Chemical and Biomolecular Engineering, The University of Sydney, Camperdown NSW 2006, Australia
[4]Faculty of Health and Medicine, The University of Sydney, Camperdown NSW 2006, Australia
[5]Mechanical and Automotive Engineering, School of Engineering, RMIT University, Bundoora, Australia

[a)]**Also at:** Department of Otolaryngology, Head and Neck Surgery, Westmead Hospital, Hawkesbury Rd, Westmead NSW 2145, Australia.
[b)]**Author to whom correspondence should be addressed:** kiao.inthavong@rmit.edu.au

ABSTRACT

Airflow through the nasal cavity exhibits a wide variety of fluid dynamic behaviors due to the intricacy of the nasal geometry. The flow is naturally unsteady and perhaps turbulent, despite Computational Fluid Dynamics (CFD) in the literature being assumed as having a steady laminar flow. Time-dependent simulations can be used to generate detailed data with the potential to uncover new flow behavior, although they are more computationally intensive than steady-state simulations. Furthermore, verification of CFD results has relied on a reported pressure drop (e.g., nasal resistance) across the nasal airway although the geometries used are different. This study investigated the unsteady nature of inhalation at flow rates of 10 l/min, 15 l/min, 20 l/min, and 30 l/min. A scale resolving CFD simulation using a hybrid Reynolds-averaged Navier–Stokes–large eddy simulation model was used and compared with experimental measurements of the pressure distribution and the overall pressure drop in the nasal cavity. The experimental results indicated a large pressure drop across the nasal valve and across the nasopharynx, with the latter attributed to a narrow cross-sectional area. At a flowrate of 30 l/min, the CFD simulations showed that the anterior half of the nasal cavity displayed dominantly laminar but disturbed flow behavior in the form of velocity fluctuations. The posterior half of the nasal cavity displayed turbulent activity, characterized by erratic fluctuating velocities, which was enhanced by the wider cross-sectional areas in the coronal plane. At 15 l/min, the flow field was laminar dominant with very little disturbance, confirming a steady-state laminar flow assumption is viable at this flow rate.

Published under license by AIP Publishing. https://doi.org/10.1063/5.0036095

I. INTRODUCTION

The nasal cavity functions to humidify and warm the air and filter it from particulates, such as bacteria and pollen, all the while allowing safe odorant gases to reach the olfactory receptors to facilitate the sense of smell. However, it is these very intricacies of the nasal cavity that make it such a complicated organ to be analyzed. Although extensive computational[1–3] and experimental[4–6] studies on the airflow behavior in the nasal cavity have been performed, some critical questions about nasal airflow remain unanswered, such as how particular variations in nasal airway geometry combined with the breathing flow rate may alter flow patterns. Doorly *et al.*'s[7,8] works provided a review and a comprehensive discussion of the relationship between nasal geometry and flow behavior of a nasal cavity, while also presenting their own experimental and computational fluid dynamics (CFD) simulation results for three

models. Qualitative images were used for insightful visualization and discussions.

Computational Fluid Dynamics (CFD) is a useful platform to study airflow in the nasal cavity. Recently, it has been used as a non-invasive method to investigate flow behavior.[9–18] Li *et al.*[19] compared results using various turbulence models against the experimental work of Hahn, Scherer, and Mozell,[4] replicating the unilateral cavity geometry with the nasopharynx omitted. The results demonstrated that a laminar flow model was most suitable for a flow rate of 180 ml/s through a single nasal chamber (21.6 l/min for both chambers) and the Large Eddy Simulations (LES) model and direct numerical simulations were better suited for unilateral flow rates of 560 ml/s and greater. This is consistent with many studies reported in the literature where a laminar flow assumption was used for flow rates of 15 l/min, or less.[1,20–24] For flow rates > 20 l/min, a turbulent flow field was assumed. Early studies applied RANS (Reynolds-averaged Navier–Stokes) models including k–ε,[25] k–ω,[26,27] and v^2–f.[28] Kleinstreuer and Zhang[29] demonstrated that to capture a laminar-transitional turbulent flow in a human airway, a low-Reynolds-number (LRN) k–ω model was suitable. This model was later adopted by other researchers.[30–32]

In nearly all the cited studies among others,[33–37] constant inhalation flow rates were modeled under steady-state conditions, which are quick to solve and therefore useful for determining consistent flow characteristics among extensive population sample studies. However, the results are time-invariant flow fields, but due to the intricate geometry of the nasal cavity, it is expected that flow fluctuations occur from either separated flow or due to turbulence. In fact, flow in the nasal cavity is most likely to experience both laminar and turbulent regimes.[7,8,38] Transient simulations made with Large Eddy Simulations (LES) can resolve both flow disturbance and turbulence. For example, Calmet *et al.*[39] presented unsteady flow dynamics during rapid inhalation, Lee *et al.*[40] simulated the entire respiratory (inhalation–exhalation) cycle, and Liu *et al.*[41] and Ghahramani *et al.*[42] investigated micrometer-sized particle deposition to overcome the deficiencies of turbulence dispersion with RANS (Reynolds-averaged Navier–Stokes) turbulence models. However, these studies did not include the corresponding experimental data for verification.

The scale up in computational costs in transition from a steady-state laminar flow to LES can be prohibitive because of the requirement of a small filtering mesh element size and the small time steps required to satisfy the criterion of $CFL < 1$. In addition, there are strict requirements for achieving a satisfactory near-wall mesh defined by the viscous wall units (x^+, y^+, z^+). While the wall-normal distance y^+ needs to be kept < 1, the spanwise and streamwise directions become equally important in respiratory airflows since the flow is much more three-dimensional than those found in standard test cases such as channel flows. However, LES studies in the respiratory airflows rarely address these requirements.

An alternative is the hybrid RANS–LES turbulence model that seeks to exploit the best features of the RANS and LES approaches and relaxes the strict requirements of the near-wall mesh. This modeling technique was developed initially for external flow (e.g., aerospace and automotive[43]) but has more recently been seen to offer significant advantages in internal flows as well.[44] The essential idea is to exploit both models in their optimal domain of application. As such, a $k-\omega$ SST model is employed close to the wall as it can capture the boundary layer well and has good separation prediction capabilities on a suitably refined near-wall mesh in SST. On the other hand, LES is best suited to modeling flow away from the walls and can capture the dynamic behavior of wakes and separated flows. These hybrid or scale resolving models have undergone much development, which has culminated in the stress blended eddy simulation (SBES) where the blending between the eddy viscosity and subgrid-scale viscosity is explicit. Given its increasing use and demonstrated benefits, it was seen as timely to apply the model to this important biomedical flow.

CFD studies require verification/validation of the solution, and this has manifested in the form of an overall pressure drop (reported in various studies).[5,27,45] The overall pressure drop is taken between the surrounding ambient air and a posterior location in the nasal cavity, usually the nasopharynx exit, or choanae. Reference 46 proposed a pressure drop relationship based on Bernoulli's equation, and despite its inviscid flow assumption, the relationship compared well with a data-fitted relationship.

In this study, we aim to characterize the fluid flow through a nasal airway at a constant flow rate using CFD. To verify the solution, experimental data (from the same nasal model) for pressure values at the lateral wall and nasal floor locations were extracted and used to compare directly with the CFD results. The overall pressure drop was compared with the reported data in the literature. For the CFD study, a scale resolving simulation with a hybrid RANS–LES model was used to characterize the flow at a constant flow rate of 15 l/min and 30 l/min, where the latter is approximately the peak inspiratory flow during a respiratory cycle.

II. METHOD

A. Nasal cavity model

A human nasal cavity model was reconstructed from CT scans of a 48-year-old Asian male through segmentation techniques. The scan resolution was 512×512 pixels^2 with a slice thickness of 0.5 mm The nasal model (labeled *NC*04 and used in previous studies)[47,48] was evaluated by a qualified clinician (ear nose throat specialist) as having a deviated septum and a narrow nasopharynx outlet. The segmentation procedure was performed using a 3D slicer. The DICOM files were imported into the 3D slicer, and a Laplacian sharpening filter was applied to enhance the image registration. Thresholding Hounsfield (HU) values of −1024 to 550 were used. Segmentation of individual anatomical regions of interest was performed and exported as an STL (stereolithography) file. The STL regions were imported into Ansys SpaceClaim where surface repair was conducted through a "shrinkwrap" technique. The segmentation produced a 3D volume computer model, and this was manually refined by reducing the effects of noise and smoothing unrealistic regions. The sinuses were omitted and truncated at their respective ostia. External facial features were included to ensure realistic inhalation at the nostrils.[21] To prevent large flow gradients forming at the nasopharynx outlet boundary, an artificial extension (50 mm in length) was added. A 3D model of 1 mm wall thickness was printed using *VisiJet SL Clear* transparent SLA resin. Externally protruding ports (2 mm in diameter) were added to the external walls to allow pressure transducers to record pressure values at spe-

Published under license by AIP Publishing

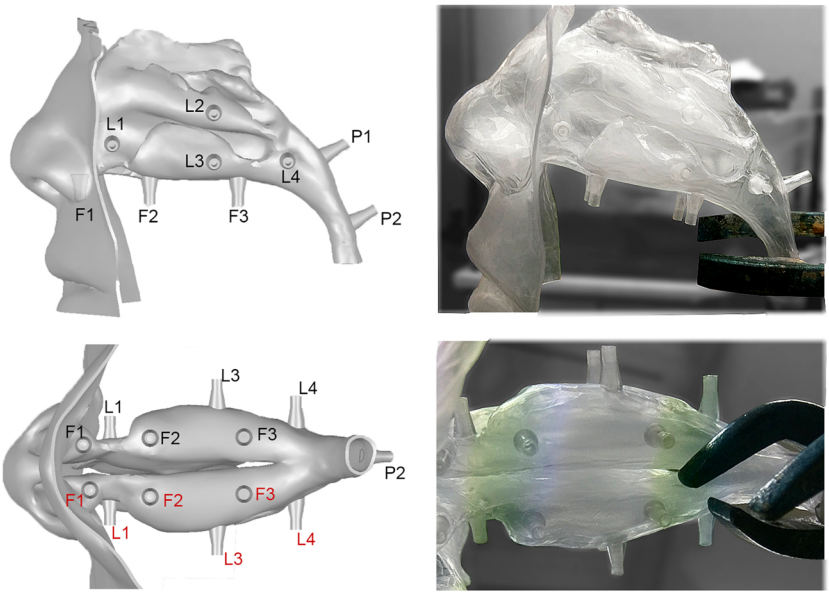

FIG. 1. Labeled schematic of the computational model showing the port locations where the pressure transducer was placed and its corresponding photo image. The port locations were placed symmetrically between the left and right cavity and labeled *L* for locations on the lateral walls and *F* for locations on the nasal floor. Location *F*1 sits along the floor of the vestibule and is hidden behind the face in the image. The two posterior ports after the left and right cavities had merged were labeled *P*1 and *P*2.

cific locations. There were three ports along the nasal cavity floor, four on the lateral walls of both sides of the nasal cavity (fourteen in total), and two additional posterior ports at the nasopharynx (refer to Fig. 1).

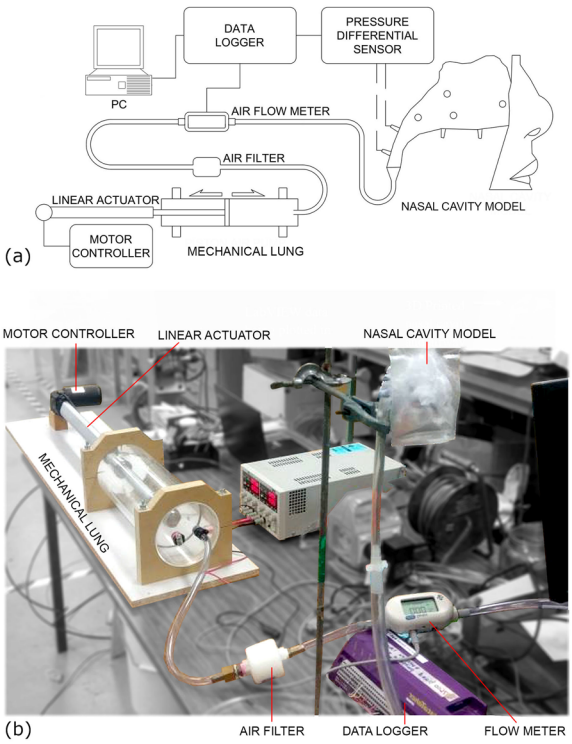

FIG. 2. Schematic and the photo of the experimental test rig setup used for pressure differential measurements.

B. Experimental pressure measurement station

The experimental setup is depicted in Fig. 2, which shows (a) a simplified schematic and (b) a photograph of the test station and the setup. A linear actuator controlled the airflow with a VNH5019 motor driver carrier and an Arduino Uno R3 programmable logic controller. The in-built pulse-width modulation (PWM) function in the Arduino sent a signal to the motor driver to alter the output voltage to the linear actuator. The flow was modulated using a pressure regulator and a flow adjustment needle valve, and a TSI4043 flow meter was used to monitor the constant flow rate. The breathing flow rates evaluated were 10 l/min, 15 l/min, 20 l/min, 30 l/min, which are typical values used in computational studies, and they are within the range of a full sinusoidal respiration (inhalation and exhalation) profile with a period of 4 s and a tidal volume of 500 ml. Sensirion SDP-1000 differential pressure transducers were used to measure the pressure drop between any two ports, totalling 16 measurements per flow rate. After a stable constant flow rate was established, data acquisition was logged at a rate of 10 Hz for 10 s and then averaged.

C. CFD modeling

CFD simulations were performed for constant inhalation flow rates for 10 l/min and 15 l/min inhalation rates using a laminar flow model,[33,49,50] while for 30 l/min inhalation, a Stress-Blended Eddy Simulation (SBES) turbulence model was used. The SBES model applies a Reynolds-averaged Navier–Stokes (RANS) model in the near wall region, while resolving the flow away from the wall with a Large Eddy Simulation (LES). Hybrid RANS–LES models, such as the SBES model, overcome the LES limitation associated with the need for very fine meshes in the wall boundary layer by integrating to the wall using a RANS model. The k-ω SST (Shear Stress Transport) model was used with the LES Wall-Adapting local Eddy-Viscosity (WALE) model for the scale resolving component. The incompressible flow equations describing the conservation for mass

Published under license by AIP Publishing

and momentum are expressed as

$$\frac{\partial}{\partial x_i}(\bar{u}_i) = 0, \tag{1}$$

$$\frac{\partial}{\partial t}(\rho\bar{u}_i) + \frac{\partial}{\partial x_j}(\rho\bar{u}_i\bar{u}_j) = -\frac{\partial\bar{p}}{\partial x_i} + \frac{\partial\sigma_{ij}}{\partial x_j} + \frac{\partial\tau_{ij}}{\partial x_j}, \tag{2}$$

where u_i is the flow velocity vector, ρ is the fluid density, p is the pressure, and σ_{ij} is the stress tensor due to molecular viscosity. The overbar $\bar{\varphi}$ on the scalar quantity φ denotes a Reynolds-averaging operation in the RANS formulation and a spatio-temporal filtering operation in the LES formulation. The turbulence stress tensor $\tau_{ij} \equiv \rho(\overline{u_i u_j} - \bar{u}_i\bar{u}_j)$ for the SBES formulation is assumed to blend between the Reynolds stress tensor $\tau_{ij}^{\mathrm{RANS}}$ for the RANS formulation and the subgrid-scale stress tensor τ_{ij}^{LES} for the LES formulation, according to the blending function

$$\tau_{ij} = f_s\tau_{ij}^{\mathrm{RANS}} + (1 - f_s)\tau_{ij}^{\mathrm{LES}}, \tag{3}$$

where $0 \le f_s \le 1$ is the shielding function.

The modeling was performed using Ansys Fluent (version 2019R3). The equations were solved using a coupled solver, which ensures very strong coupling between the pressure and velocity fields. The convective terms were resolved using second-order bounded schemes, and time-stepping was performed using the bounded second-order implicit scheme. Gradients were calculated

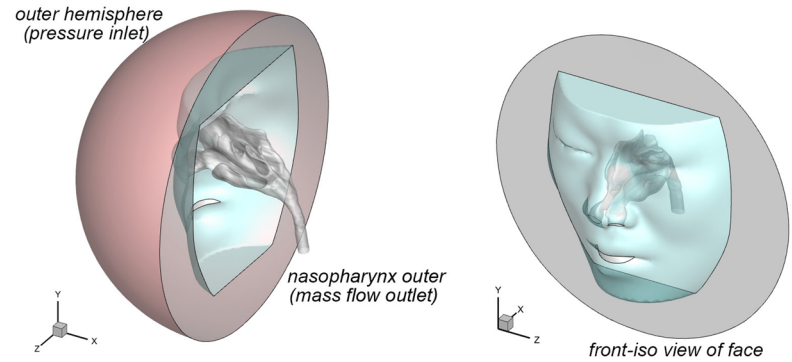

(a) Computational domain

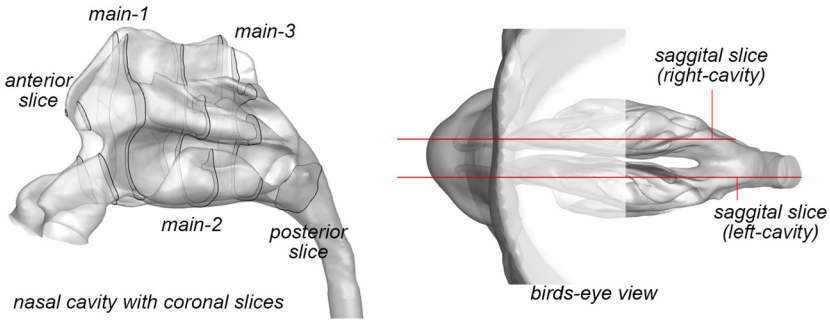

(b) Coronal and sagittal slices

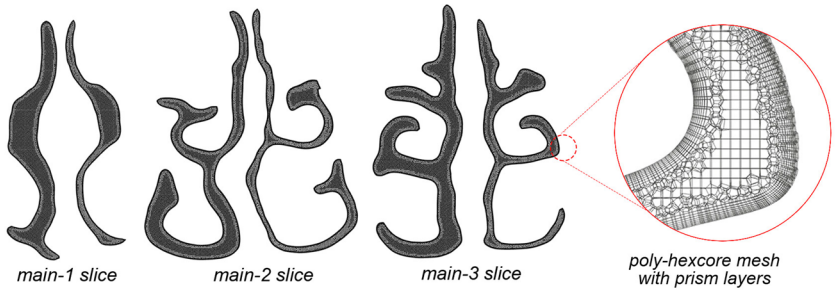

(c) Internal mesh

FIG. 3. Nasal cavity geometry showing the computational domain that includes (a) the outer face and an outer hemisphere. Planar slices were created for post-processing steps. The nasal cavity is shown with coronal slice locations. The slices cutting through the anterior, main passage, and posterior locations are shown. Two sagittal slices were cut through each nasal cavity (left and right) side. (c) The internal mesh of main-1, main-2, and main-3 is shown, and a zoomed-in view of the mesh shows 8-prism layers and an internal hexahedral cell with a length of 0.2 mm, i.e., volume = 8.0×10^{-12} m^3.

Published under license by AIP Publishing

using the least-squares cell-based method, and the pressure was discretized using a second-order scheme. Default under-relaxation factors were employed. A laminar model was used for flow rates of 10 l/min and 15 l/min. For 30 l/min, the hybrid RANS–LES model was used, where the hemisphere dome [see Fig. 3(a)] was a pressure inlet with a turbulence intensity of 5% and a viscosity ratio of 10, while the nasopharynx outlet was a mass flow boundary condition.

D. Meshing and time step requirements

The LES component of the SBES model required a sufficiently fine mesh to resolve the large eddies. The model was meshed with a polyhedral mesh on its surface, filled with hexahedrons in the bulk flow region, and this mesh was connected to the inflation via polyhedra. Eight prism layers were placed on the walls where the normalized wall distance $y^+ < 1$ on all walls. The strict requirements of normalized wall distances x^+ and z^+ were not required for the SBES model. Three meshed models were evaluated, as summarized in Table I, where the hexahedral cell length was $\Delta = 0.3$ mm, 0.2 mm, and 0.15 mm, with eight prism layers set with first cell heights of 10% of Δ.

To ensure sufficient spatial resolution was achieved, the mesh was evaluated based on the turbulence integral length-scale, which includes most of the energy containing eddies and is estimated from a precursor $k-\omega$ SST model simulation using

$$l_o = \frac{k^{1.5}}{\varepsilon} = \frac{k^{0.5}}{C_\mu \omega}, \qquad \text{where } C_\mu = 0.09. \tag{4}$$

Based on Kolmogorov's energy spectrum, 80%–90% of the turbulence kinetic energy can be resolved by the largest eddies if approximately five to twelve cells in each direction are created for an eddy with scale l_o. The mesh analysis through contour plots of the coronal slices indicated that 5–10 cells were found.

The time-step size also needs to resolve the energy-containing eddies. An estimate of the time resolution of the model was calculated based on the time scale defined as

$$\lambda_g/u' = (15\nu/\varepsilon)^{1/2} = \sqrt{15}\tau_\eta,$$

where the minimum value was $\tau_\eta = 5.0 \times 10^{-5}$ s. A smaller value of $\tau_\eta = 2.0 \times 10^{-5}$ s was used to ensure the time resolution was sufficient to establish a scale resolved flow field.

A precursor steady-state RANS simulation was performed to establish the flowfield. The simulation was then switched to transient and simulated for 0.15 s to allow the scale resolving components to establish. Monitoring points were located on five coronal planes, and data sampling began recording for velocity, pressure, and resolved and unresolved turbulence kinetic energy components. The monitoring points sampled for a period of 0.20 s, and the simulation ended after 0.35 s. The Reynolds and Womersley numbers near the nasopharynx were calculated as 1690 and 2.44, respectively, based on the values of $D_h = 0.0149$ m, $U = 1.66$ m/s, $\rho = 1.225$ kg/m^3, $\mu = 1.79 \times 10^{-5}$ Pa.s, and $\omega = 2\pi f = 1.57$ s^{-1} based on a nominal breathing frequency corresponding to approximately 15 breaths per minute.

TABLE I. Summary of different mesh resolution parameters, where N_{cells} is the number of mesh cells/elements, Δ is the grid size, N_{pl} is the number of prism layers, and h_{pl} is the height of the first prism layer.

Mesh	$N_{cells}(\times 10^6)$	Δ (mm)	N_{pl}	h_{pl} (mm)
Mesh1	3.7	0.30	8	0.03
Mesh2	8.1	0.20	8	0.02
Mesh3	11.8	0.15	8	0.015

Non-dimensional values of the grid spacing were evaluated with the preliminary results and were based on the integral length scale calculated from the cross-sections shown in Fig. 6, giving a normalized grid spacing of $\Delta^+ = 0.583$. The turbulence time scale is estimated by $\tau_\eta = \sqrt{\nu/\varepsilon}$, giving $t^+ = 0.0536$.

III. RESULTS

A. Pressure distribution and pressure drop comparison

The pressure differentials between the ambient air and port locations from the experimental and CFD results are given in Fig. 4. The plots combine the pressure distribution in the left (black color), the right (red color), and the posterior (blue color) nasal cavity. The pressure differentials were slightly higher along the lateral walls (labeled L1 to L4) than along the floor locations (labeled F1 to F3) while the right cavity (with a larger flow rate moving through) exhibited greater pressure differential values than the left cavity.

A large pressure drop occurred between the posterior positions P1 and P2 caused by the severe narrowing of the nasopharynx cross-sectional area, which is not typically representative of the population. The cross-sectional area at the posterior slice [see Fig. 3(b)] was $A_c = 1.737$ cm^2, which reduces to $A_c = 0.575$ cm^2 at the nasopharynx outlet (horizontal plane). The pressure drop across the nasal valve is best represented by the difference between locations F1 and F2, and this also showed a large value. The CFD results for the pressure distribution showed a generally good match with the experimental data where the discrepancies depicted CFD results with a higher pressure drop than the experimental values, particularly in the left cavity for a flow rate of 30 l/min.

Figure 5 shows the overall pressure drop between the ambient and the posterior locations P1 and P2, obtained from the CFD and experimental results. The results from the two posterior locations were given to demonstrate the sensitivity of the results when the nasopharynx exhibits a sharp reduction in the cross-sectional area. A comparison with the experimental data of Kelly *et al.*,[5] Weinhold and Mlynski,[45] and Segal, Kepler, and Kimbell[51] and computational results of Subramaniam *et al.*,[1] Ge, Inthavong, and Tu,[23] Wen *et al.*,[27] and Inthavong, Shang, and Tu[46] is shown, which showed that the pressure drop between the ambient and location P1 was most consistent with the reported data and follows the trend-line from Inthavong, Shang, and Tu.[46] Each nasal geometry is unique, and therefore, the overall pressure drop represents an overall flow resistance in their respective nasal geometry and neglects local influences.

B. Mean velocity contours

The mean and RMSE (Root Mean Square Error) velocity magnitude contours were taken at multiple slices in the three anatomical planes (i.e., sagittal, transverse, and coronal), as shown in Fig. 6. The RMSE is defined as the root mean square of the difference between

Published under license by AIP Publishing

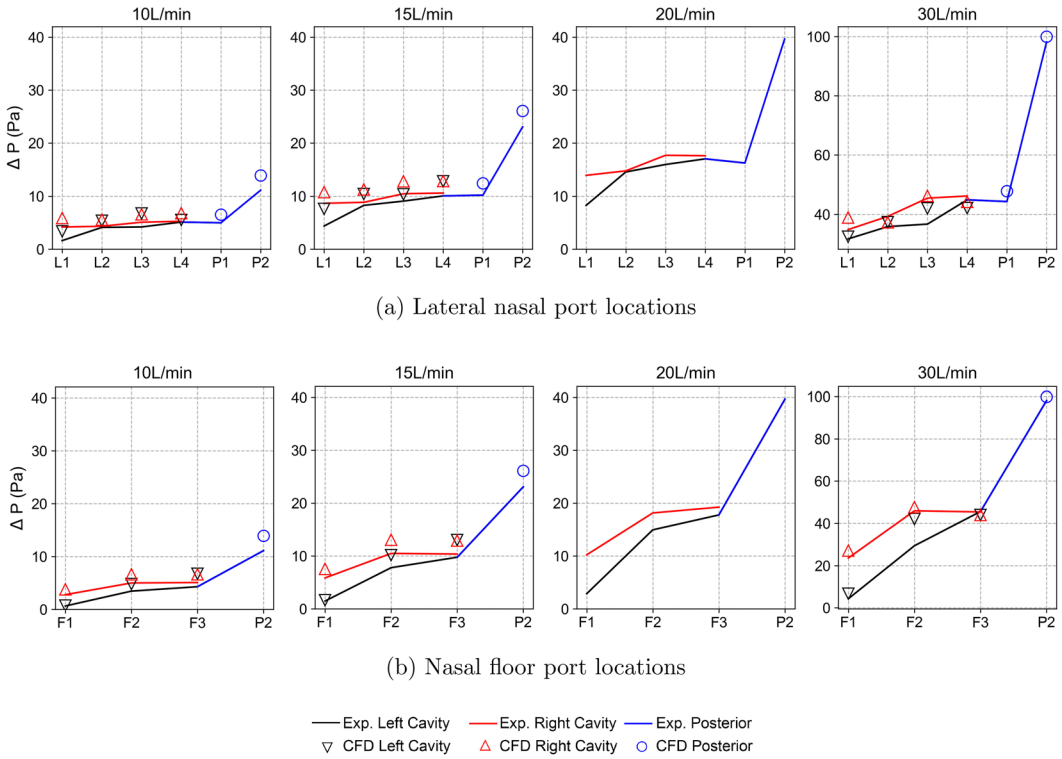

FIG. 4. Pressure differential between ambient surrounding air and port locations (a) at the lateral walls labeled L1 to L4 and (b) along the nasal floor labeled F1 to F3 (see Fig. 1 for location definitions). The lines and markers are colored by the airway side, where black denotes the left cavity, red denotes the right cavity, and blue denotes the posterior region where there is a single passageway only. CFD simulations were performed for flow rates of 10 l/min, 15 l/min, 20 l/min, and 30 l/min.

the instantaneous velocity and the average velocity, given as

$$RMSE = \sqrt{\frac{1}{N}\sum_{i=1}^{N}(u_i - \overline{u})^2},$$

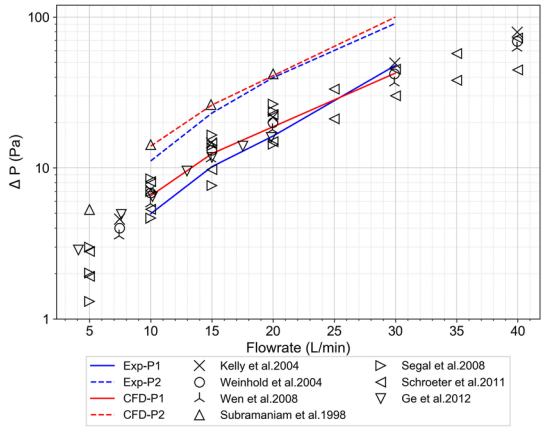

FIG. 5. Overall pressure drop from the ambient air and posterior locations P1 and P2 (see Fig. 1 for location definitions) compared with literature data.[1,5,23,27,45,51] Line data of Inthavong *et al.*[46] use the equation $\Delta P = (0.2033\sqrt{\rho}A^{-1}Q + 0.338\sqrt{\rho}A^{-1}Q_0)^2$, where $\rho = 1.225$ kg/m^3, A is per unit area in m^2, Q is the flowrate, and Q_0 is a unit flow rate.

which represents the spread of the velocity magnitude. It can be used as an index of comparison to identify where the main regions of instantaneous velocity deviated from mean results.

Two sagittal planes, one through the left and the other through the right cavities, demonstrate the streamwise flow direction, which therefore represents the main flow path. The flow accelerates through the nasal valve region directed at an approximate direction of 45° before impinging on the middle turbinate. The transverse planes show the flow paths in the lateral directions, where at mid-height (y-midplane), the flow separates into two streams, with one moving laterally and the other moving along the septal wall [denoted by the arrows in Fig. 6(c)]. The coronal planes showed high velocities occurring in the anterior plane and the bulk flow remaining in the inferior half and then the middle regions of the main nasal passage. The superior locations where the olfactory region lies experience low flow velocities. Furthermore, the main deviations are found in the right cavity where most of the flow moves through due to the larger cross-sectional area. Locally, the deviations occur in the middle region of the "main-1" and "main-3" coronal planes and the posterior plane.

C. Flow characteristics in the nasal cavity

The instantaneous velocity contours were taken at $t = 0.20$ s (after the flow had been established) and are shown in Fig. 7(a). Fluctuations were found in the nasopharynx, along the nasal floor, and the nasal septum wall. Using these contours as a basis of the flow

Published under license by AIP Publishing

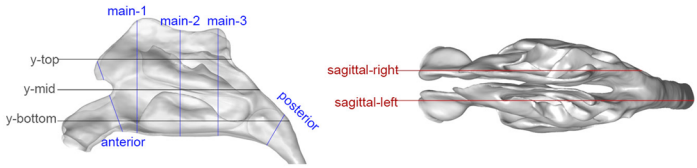

(a) All slice locations, e.g., coronal, sagittal, and transverse

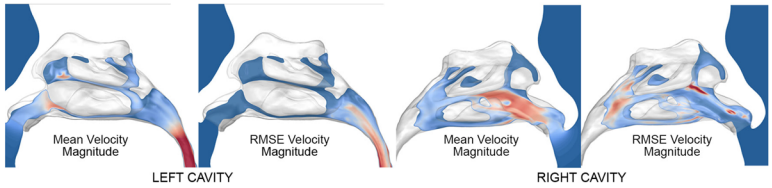

(b) Velocity contours in the sagittal planes

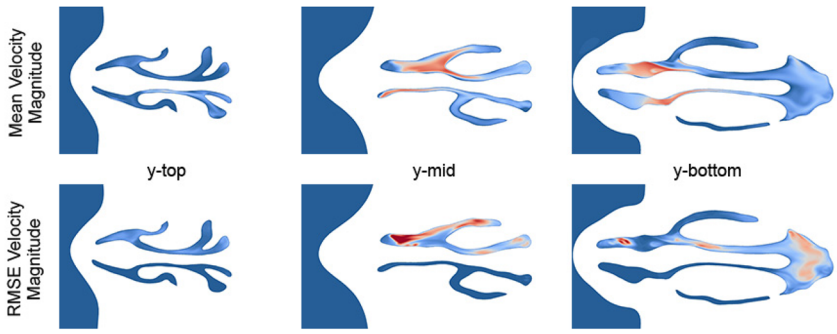

(c) Velocity contours in the transverse planes

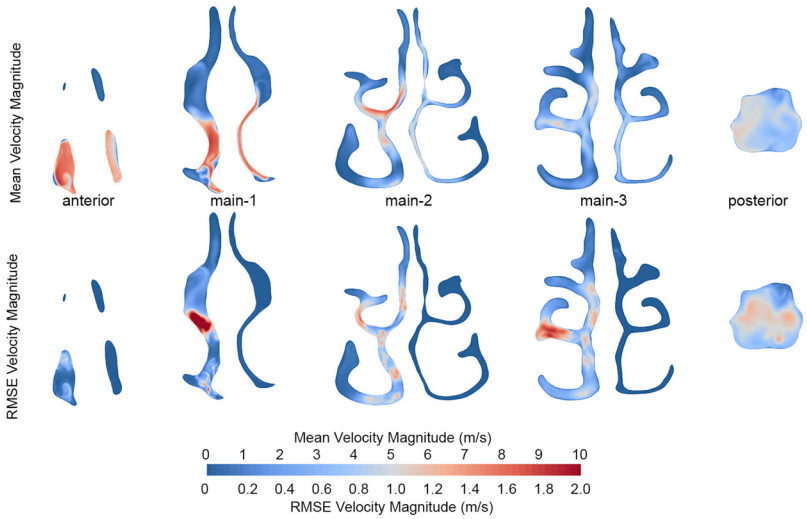

(d) Velocity contours in the coronal planes

FIG. 6. (a) Cross-sectional plane locations and (b) mean and RMSE velocity contours shown at the sagittal (c) transverse and (d) coronal planes.

field, velocity vectors are shown in Fig. 7(b) and labeled *a* to *e* with key flow features. This includes (a) flow entering the nostril that is directed at an approximate angle of 40° and (b) the air impinges on the anterior septum where the majority of the air moves through the inferior half of the main nasal passage. (c) A recirculating flow was found past the vestibule notch caused by flow separation. (d) The flow that is directed superiorly also impinges onto the head of the middle turbinate. (e) Posteriorly, multiple flow streams mix,

Published under license by AIP Publishing

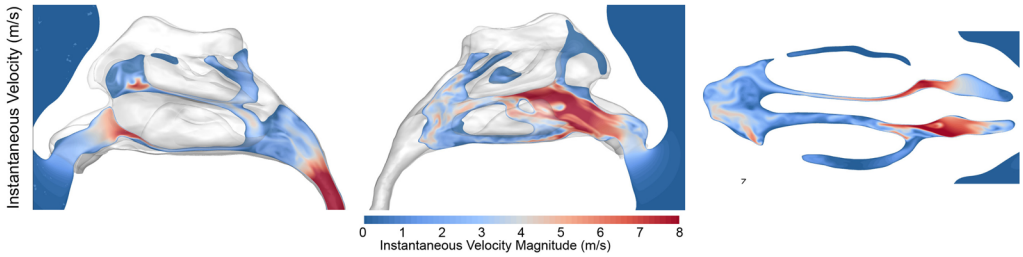

(a) Instantaneous velocity contours

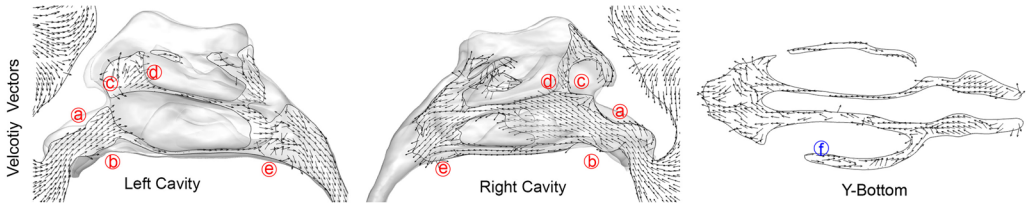

(b) Instantaneous velocity vectors

FIG. 7. (a) Instantaneous velocity contours taken on the sagittal and transverse planes and (b) velocity vectors where labels circled in red highlight key flow characteristics.

creating a highly turbulent and disturbed flow. (f) On the very lateral and posterior regions of the inferior turbinates, the vectors exhibit reverse flow where the flow is returning toward the front of the nose, although this is at a very low velocity.

Flow streamlines have been depicted in past studies either as sketches[1,3,52] or extracted CFD images[27,38] and are shown in Fig. 8, which indicates some common flow features despite the different nasal cavity models. These include a disturbed flow in the vestibule, two streams that separate from the nasal valve region, a recirculating region in the superior anterior nasal notch, and three streams converging at the choana to form a highly mixed region in the entrance into the nasopharynx. The path lines in the current CFD study were taken at a particular time instant (t = 0.20 s), and this was able to reveal temporal disturbances in the labeled (red arrows, also see the video in the supplementary material) stream paths.

D. Fluctuation analysis

Transient monitoring points located at each coronal slice recorded velocity and turbulence kinetic energy over a time period t = 0.16 s–0.35 s are shown in Fig. 9. The velocity magnitudes in "anterior" and "main-1" were of the order of 8 m/s in the right nasal cavity and 6–7 m/s in the left nasal cavity. The fluctuations were negligible in the left cavity. The fluctuations in the right cavity exhibited small amplitudes (a peak of 0.15 m/s) and showed an ordered repeating pattern. The spectral analysis of the velocity fluctuation showed a dominant frequency occurring at f = 184 Hz, which is a manifestation of the flow separation from the upstream vestibule. Doorly *et al.*[7] found that flow separation in a more superior location displayed a regular frequency of approximately 460 Hz. These regular frequencies confirm a laminar disturbed flow behavior. The planes "main-2, main-3," and "posterior" exhibited much lower velocity magnitudes but higher amplitudes and less well ordered repeating patterns. In these planes, there was an increase in the dominant frequencies, and in the "posterior" plane, there was no order at all.

A power spectral density analysis was created by determining the turbulence kinetic energy, k. The resolved component of k, produced by the large eddies, was obtained from the velocity fluctuations monitored at each point given in Fig. 9, over the monitoring period of 0.4 s. The unresolved k produced by the small eddies (that were smaller than the sub-grid scale) were explicitly modeled. This unresolved turbulence component was assumed isotropic and calculated by $k_u = (C_w \Delta S)^2/0.3$, where Δ is the grid length scale and C_w = 0.325 in the WALE model. A fast-Fourier-transform was applied to the data from each monitored point to produce the power spectrum. The spectral analysis of the turbulence kinetic energy identified how much of the inertial sub-range was resolved by comparing the gradient $-5/3$, which is associated with the range of frequencies in which the energy cascade takes place. It is dominated by inertial energy transfer, where energy production is equal to the energy dissipation. This behavior was most evident and strongly correlated in the monitoring points found at main-2, main-3, and "posterior," suggesting a strong presence of turbulence in this posterior half of the nasal cavity.

A similar analysis was performed for a lower flow rate of 15 l/min since at this flow rate, a laminar flow assumption, using the "*laminar*" viscous model (absence of turbulence), is commonly adopted[50,53,54] but without justification. Figure 10 demonstrates a relatively constant flow with an absence of fluctuating velocities except for some minor changes in the posterior region. This suggests that the locations monitored exhibited very orderly flow behavior that is characteristic of a laminar flow.

IV. DISCUSSION

Nasal airway resistance is deduced from the pressure drop by the relationship $R = \Delta P/Q$, where Q is the flowrate with units

Published under license by AIP Publishing

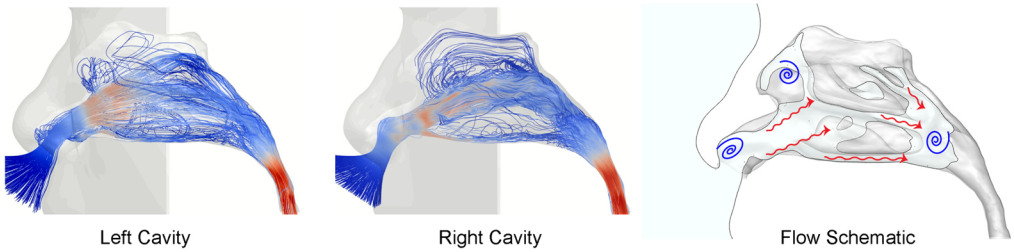

(a) Streamlines and an overall flow schematic of the CFD results

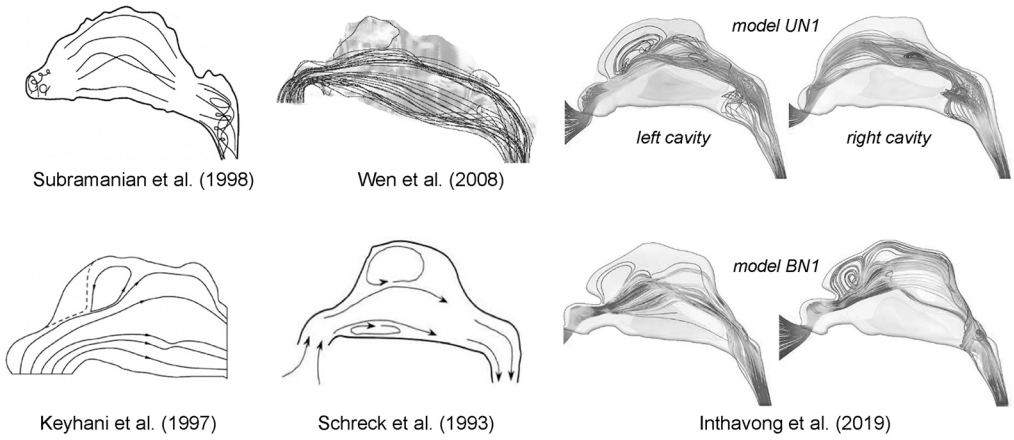

(b) Comparative streamlines reported in the literature

FIG. 8. (a) Path lines in the left and right cavity showing the flow behavior and identifying recirculating flow regions and a schematic summarizing the main flow features. (b) Reported streamline schematics or CFD simulation results found in the literature for comparison.

of mL/s for unilateral airflow resistance and $R_T = (R_L + R_R)/R_L R_R$ (parallel resistance form) for bilateral airflow resistance, where the subscripts L and R represent the left and right cavities, respectively. Our results produced resistance values of 0.03 Pa s/ml, 0.04 Pa s/ml, 0.05 Pa s/ml, and 0.09 Pa s/ml for flow rates of 10 l/min, 15 l/min, 20 l/min, and 30 l/min, respectively. Comparatively, Bruning *et al.*[55] found a median value of 0.05 Pa s/ml for 12 l/min, and Borojeni *et al.*[15] found a range of 0.017 – 0.12 Pa s/ml for bilateral resistance at 15 l/min.

A primary cause for resistance is undoubtedly constrictions in the geometry. The relationship between flow resistance and a characteristic area have been proposed by Sanmiguel-Rojas *et al.*[56] [nostril area, $R = f(A_{nostril})$] and Garcia *et al.*[57] [minimum cross-sectional area $R = f(A_{min})$]. Garcia *et al.*[57] found that when the airway constriction, defined by the minimum cross-sectional area, is severe enough, the resistance at the constriction overwhelms the resistance of all other regions of the nasal cavity. Their model used a pressure drop of 19 Pa, which yielded approximately 15 l/min (250 ml/s). This correlates with the nasal valve region, which has been identified as the minimum cross-sectional area attributing to more than 50% of total airway resistance.[58] In addition, Hildebrandt *et al.*[59] and Bruning *et al.*[55] found a maximal pressure gradient (decreasing) at the isthmus nasi on an average in nasal geometry from 25 patient models. The present study confirmed a high resistance across the nasal valve region (from location F1 to F2). The pressure drop across the nasal valve as a proportion of the overall pressure drop to posterior location P1 showed (see appendix A for table of values) its contribution as 56%–74% in the left cavity and 37%–47% in the right cavity for the flow rates investigated. The nasal valve has been implicated as a source of high flow resistance due to its reduced cross-sectional area producing a converging-diverging type passageway. There was also a significant pressure drop at the nasopharynx region, and this was due to the abnormally narrow cross-sectional area, suggesting that patients with this condition are expected to experience high shear stress loadings in the back of the nose. A shift in nasal patency perception may be felt in the posterior nose rather than in the nasal valve region. The results demonstrated that a reduction in the cross-sectional area in other regions would cause a secondary local region of high resistance.

The RMSE values showed significant deviations of instantaneous flow relative to its mean flow occurring at the nasal valve exit and in the middle turbinate regions. These deviations suggest strong disturbed flow features not captured in time-averaged flows. Their presence is expected to have an enhanced effect on the air

Published under license by AIP Publishing

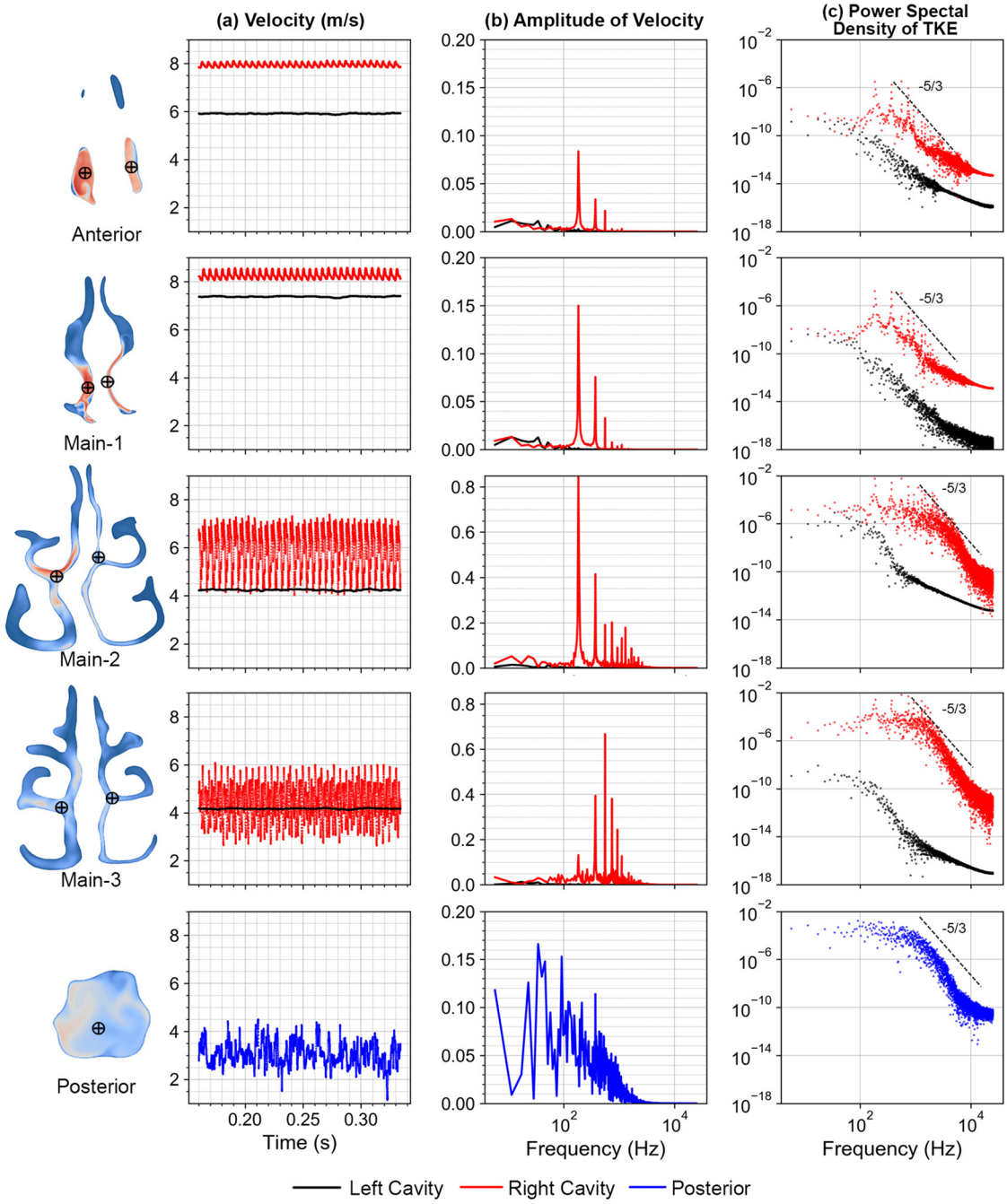

FIG. 9. Transient monitor data for (a) velocity magnitude, (b) spectral analysis of the velocity, and (c) spectral analysis of turbulence kinetic energy. The monitoring points were located in the coronal planes and monitored over the time period t = 1.6 s–2.0 s. The turbulence kinetic energy, $k = k_r + k_u$, was obtained from the resolved component $k_r = 0.5(\overline{u'^2} + \overline{v'^2} + \overline{w'^2})$ and the unresolved component $k_u = (C_w \Delta S)^2/0.3$, where Δ is the grid length scale and C_w = 0.325 in the WALE model.

conditioning capacity of the nose and particle dispersion and deposition in these local regions. There is also significant mixing in the nasopharynx due to the two air streams from the left and right cavities merging in a converging passageway.

Transient monitoring of data at points throughout the nasal cavity allowed more detailed information of the flow field than in a steady flow. The left nasal cavity was narrower, and the flow was laminar and exhibited negligible fluctuations. The right cavity was

Published under license by AIP Publishing

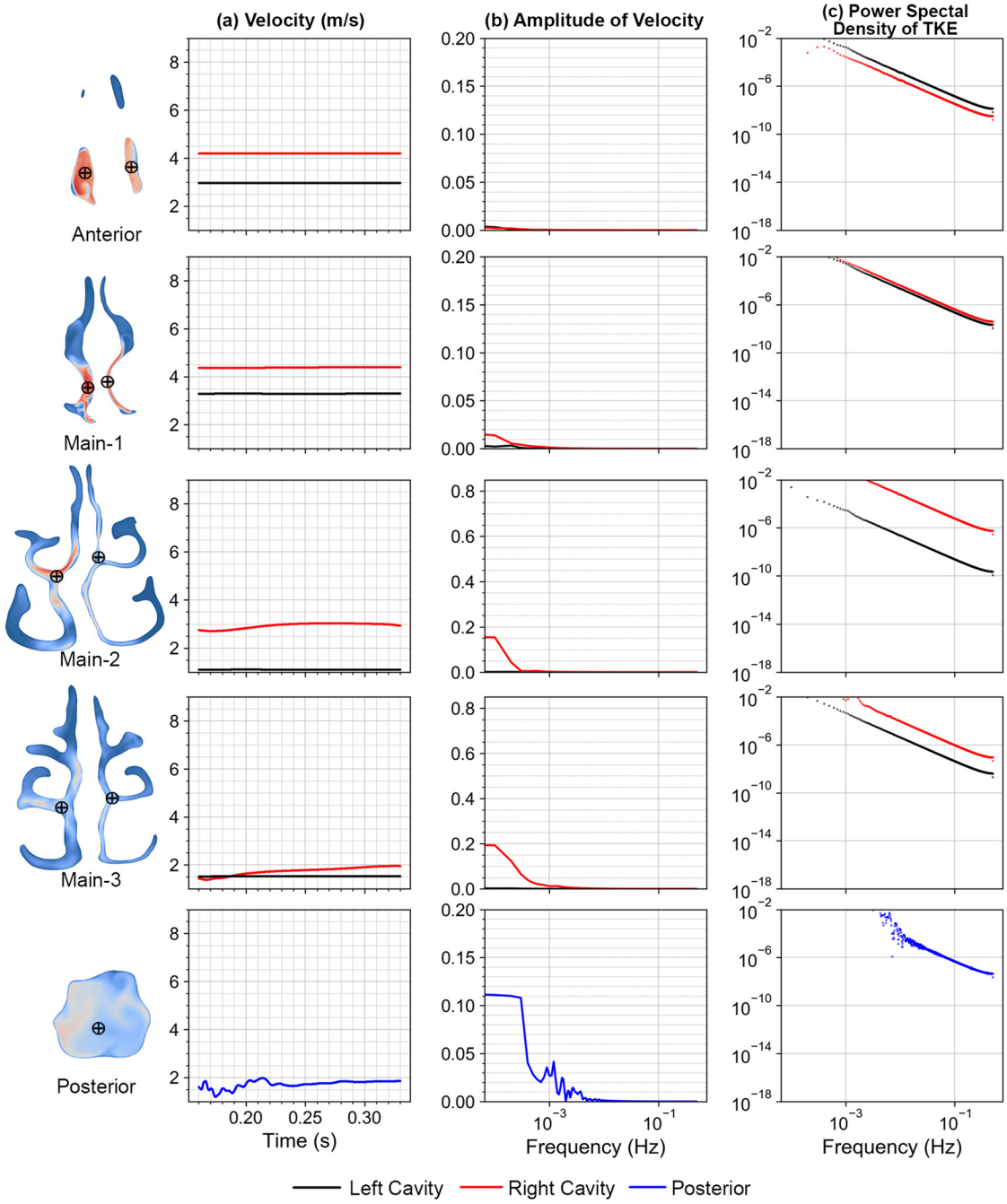

FIG. 10. Transient monitor data at the same locations and setup as in Fig. 9, except for the flow rate, which is now 15 l/min: (a) velocity magnitude, (b) spectral analysis of the velocity, and (c) spectral analysis of turbulence kinetic energy.

the more patent airway and showed higher velocities and fluctuations. In the anterior half, the monitored points exhibited cyclic fluctuations with a dominant frequency of 184 Hz (see animations in the supplementary material). Spectral analysis of the turbulence kinetic energy showed a weak correlation with the −5/3 slope, suggesting a small contribution of turbulence in the inertial sub-range of the anterior half, and it showed that the fluctuations were dominated by a disturbed laminar flow from flow separation. We note that only one monitoring point in the middle of the coronal plane was taken and that different levels of turbulence could exist in other regions. In the posterior half of the nasal cavity where the airway cross section increased, the fluctuations were much more significant,

Published under license by AIP Publishing

TABLE II. Pressure distribution values extracted from experimental measurements and CFD simulation results.

	Experimental, flow rates				CFD, flow rates		
Location	10 (l/min)	15 (l/min)	20 (l/min)	30 (l/min)	10 (l/min)	15 (l/min)	30 (l/min)
L1 left	1.59	4.35	8.24	31.64	3.33	7.59	32.43
L2 left	4.08	8.24	14.55	35.81	5.34	10.37	37.33
L3 left	4.17	9.05	15.96	36.65	6.70	10.36	41.99
L4 left	5.09	10.04	17.03	44.85	5.51	12.76	42.03
P1	4.96	10.17	16.25	44.27	6.52	12.42	47.78
P2	11.11	23.07	39.64	98.15	13.93	26.09	99.95
L1 right	4.16	8.64	13.92	34.79	5.84	10.73	38.87
L2 right	4.30	8.82	14.76	39.26	5.55	11.24	37.20
L3 right	5.07	10.44	17.70	45.42	6.56	12.79	46.17
L4 right	5.24	10.57	17.62	46.15	6.77	12.85	44.20
F1 left	0.63	1.47	2.86	4.28	0.70	1.61	6.70
F2 left	3.45	7.78	14.93	29.37	4.81	10.14	41.99
F3 left	4.28	9.75	17.75	45.58	6.75	13.01	43.93
F1 right	2.77	5.84	10.21	23.58	3.79	7.52	27.14
F2 right	4.99	10.47	18.12	45.93	6.61	13.05	47.62
F3 right	5.07	10.36	19.22	45.38	6.65	12.88	44.00
Pressure drop contributions							
Nasal Valve (*F2–F1*) Pa							
Left (Pa)	2.8	6.3	12.1	25.1	4.1	8.5	35.3
Right (Pa)	2.2	4.2	6.1	20.8	2.5	4.5	12.3
Nasal Valve (*F2–F1*) *to P1 Contribution*%							
Left (%)	56.8	62.0	74.3	56.7	63.1	68.6	73.9
Right (%)	43.9	40.9	37.3	47.1	38.3	36.4	25.8

the number of frequency modes increased, and the spectral analysis identified the turbulence energy cascade (inertial sub-range) region, to confirm the latter half of the nasal cavity exhibited very strong turbulent flow behavior.

At a lower flow rate of 15 l/min, researchers have commonly adopted a laminar flow assumption without justification. The spectral analysis of the transient velocity values monitored at nine locations indicates that a laminar model is justified for a steady simulation at 15 l/min. It was also evident that the larger cross-sectional area found at the nasopharynx is a significant contributor toward the onset of flow disturbances in the bulk flow region (Table II).

The results presented here were for a single model, which is a limitation of the work where larger samples of data through multiple models would strengthen the work. Nevertheless, one consistent trend we found that is common regardless of different patient models is the constrictive nasal valve region and its significant contribution to airway resistance. Furthermore, the narrow nasopharynx (and in fact any constrictive regions) will be a further contributor toward airway resistance.

V. CONCLUSION

Experimental measurements determined the pressure distribution across the nasal walls, and this was matched very well with the CFD simulations. The pressure drop across the nasal valve was 56%–74% in the left (congested) cavity and 37%–47% in the right (patent) cavity, when the nasopharynx bend was excluded. The nasopharynx in this study exhibited an abnormally significant cross-sectional area reduction, also leading to a large pressure drop. The nasal valve has been implicated as the primary contributor for airway resistance due to its rapid decrease in the cross-sectional area, and this phenomenon was consistent for the nasopharynx bend.

A transient scale resolving simulation using the hybrid RANS–LES k–ω SBES turbulence model was used to explore the flow features through the nasal cavity in detail. The results demonstrated separated flows leading to a mix of disturbed laminar to low-level turbulence flow in the anterior half of the nasal cavity and a highly turbulent flow in the posterior half. As the flow entered the nostril, it was directed superiorly at an approximate angle of 40°, where it impinged on the septum and moved through the inferior half of the main nasal passageway before hitting the head of the middle turbinate. There was a recirculating flow above the vestibule notch due to flow separation. At the posterior nasal cavity, upstream jets converged into one intense mixing conduit before entering the nasopharynx. Instantaneous flow fields demonstrated temporal disturbances with fluctuating flow in the nasopharynx, along the nasal floor and the nasal septum. A novelty of this work was the direct comparison of experimental measurements with a computational

Published under license by AIP Publishing

study that used a hybrid RANS–LES turbulence model, where we identified geometric features leading to flow separation and regions of laminar flow (in the anterior half) and turbulent flow behavior (in the posterior half) of the nasal cavity. Larger model samples would strengthen these results in the future.

SUPPLEMENTARY MATERIAL

See the supplementary material for the following:
S1: Velocity fluctuation animation

1. Animation 1: Velocity magnitudes at a flow rate of 30 l/min in the coronal planes over the monitoring period that is analyzed in Fig. 9.
2. Animation 2: Velocity magnitudes at a flow rate of 30 l/min in the sagittal planes over the monitoring period that is analyzed in Fig. 9.

S2: Pressure distribution data
Tabulated data of the measured and CFD simulated pressure distribution across the nasal cavity.
S3: CAD geometry of the nasal cavity for 3D printing.
A print-ready STL file of the 3D nasal cavity model with pressure ports depicted in Fig. 3.
S4: CAD geometry of the nasal cavity used for CFD analysis.
An STL file of the 3D nasal cavity model ready for CFD meshing.

ACKNOWLEDGMENTS

The authors gratefully acknowledge the financial support provided by the Garnett Passe and Rodney Williams Memorial Foundation, Conjoint Grant No. 2019-22.

DATA AVAILABILITY

The data that support the findings of this study are available within the article and its supplementary material.

REFERENCES

[1]R. Subramaniam, R. Richardson, K. Morgan, J. Kimbell, and R. Guilmette, "Computational fluid dynamics simulations of inspiratory airflow in the human nose and nasopharynx," Inhalation Toxicol. **10**, 91 (1998).
[2]D. Elad, R. Liebenthal, B. L. Wenig, and S. Einav, "Analysis of air flow patterns in the human nose," Med. Biol. Eng. Comput. **31**, 585 (1993).
[3]K. Keyhani, P. W. Scherer, and M. M. Mozell, "Numerical simulation of airflow in the human nasal cavity," J. Biomech. Eng. **117**, 429 (1995).
[4]I. Hahn, P. W. Scherer, and M. M. Mozell, "Velocity profiles measured for airflow through a large-scale model of the human nasal cavity," J. Appl. Physiol. (1993).
[5]J. T. Kelly, B. Asgharian, J. S. Kimbell, and B. A. Wong, "Particle deposition in human nasal airway replicas manufactured by different methods. Part I: Inertial regime particles," Aerosol Sci. Technol. **38**, 1063 (2004).
[6]Y. Cheng, T. Holmes, J. Gao, R. Guilmette, S. Li, Y. Surakitbanharn, and C. Rowlings, "Characterization of nasal spray pumps and deposition pattern in a replica of the human nasal airway," J. Aerosol Med. **14**, 267–280 (2001).
[7]D. J. Doorly, D. J. Taylor, A. M. Gambaruto, R. C. Schroter, and N. Tolley, "Nasal architecture: Form and flow," Philos. Trans. R. Soc. A **366**, 3225 (2008).
[8]D. J. Doorly, D. J. Taylor, and R. C. Schroter, "Mechanics of airflow in the human nasal airways," Respir. Physiol. Neurobiol. **163**, 100–110 (2008).
[9]K. Inthavong, "From indoor exposure to inhaled particle deposition: A multiphase journey of inhaled particles," Exp. Comput. Multiphase Flow **2**, 59 (2020).
[10]X. Xu, J. Wu, W. Weng, and M. Fu, "Investigation of inhalation and exhalation flow pattern in a realistic human upper airway model by PIV experiments and CFD simulations," Biomech. Model. Mechanobiol. **19**, 1679 (2020).
[11]J. Ormiskangas, O. Valtonen, I. Kivekäs, M. Dean, D. Poe, J. Järnstedt, J. Lekkala, T. Harju, P. Saarenrinne, and M. Rautiainen, "Assessment of PIV performance in validating CFD models from nasal cavity CBCT scans," Respir. Physiol. Neurobiol. **282**, 103508 (2020).
[12]L. de Gabory, M. Kérimian, Y. Baux, N. Boisson, and L. Bordenave, "Computational fluid dynamics simulation to compare large volume irrigation and continuous spraying during nasal irrigation," Int. Forum Allergy Rhinol. **10**, 41 (2020).
[13]O. Pourmehran, M. Arjomandi, B. Cazzolato, F. Ghanadi, and Z. Tian, "The impact of geometrical parameters on acoustically driven drug delivery to maxillary sinuses," Biomech. Model. Mechanobiol. **19**, 557 (2020).
[14]E. Moreddu, L. Meister, A. Dabadie, J. M. Triglia, M. Médale, and R. Nicollas, "Numerical simulation of nasal airflows and thermal air modification in newborns," Med. Biol. Eng. Comput. **58**, 307 (2020).
[15]A. A. Borojeni, G. J. Garcia, M. G. Moghaddam, D. O. Frank-Ito, J. S. Kimbell, P. W. Laud, L. J. Koenig, and J. S. Rhee, "Normative ranges of nasal airflow variables in healthy adults," Int. J. Comput. Assisted Radiol. Surg. (2020).
[16]D. O. Frank-Ito, J. S. Kimbell, A. A. Borojeni, G. J. Garcia, and J. S. Rhee, "A hierarchical stepwise approach to evaluate nasal patency after virtual surgery for nasal airway obstruction," Clin. Biomech. **61**, 172 (2019).
[17]T. Radulesco, L. Meister, G. Bouchet, J. Giordano, P. Dessi, P. Perrier, and J. Michel, "Functional relevance of computational fluid dynamics in the field of nasal obstruction: A literature review," Clin. Otolaryngol. **44**, 801 (2019).
[18]R. Huang, A. Nedanoski, D. F. Fletcher, N. Singh, J. Schmid, P. M. Young, N. Stow, L. Bi, D. Traini, E. Wong, C. L. Phillips, R. R. Grunstein, and J. Kim, "An automated segmentation framework for nasal computational fluid dynamics analysis in computed tomography," Comput. Biol. Med. **115**, 103505 (2019).
[19]C. Li, J. Jiang, H. Dong, and K. Zhao, "Computational modeling and validation of human nasal airflow under various breathing conditions," J. Biomech. **64**, 59 (2017).
[20]K. Zhao, P. W. Scherer, S. A. Hajiloo, and P. Dalton, "Effect of anatomy on human nasal air flow and odorant transport patterns: Implications for olfaction," Chem. Sens. **29**, 365 (2004).
[21]Y. D. Shang, K. Inthavong, and J. Y. Tu, "Detailed micro-particle deposition patterns in the human nasal cavity influenced by the breathing zone," Comput. Fluids **114**, 141 (2015).
[22]G. J. Garcia, N. Bailie, D. A. Martins, and J. S. Kimbell, "Atrophic rhinitis: A CFD study of air conditioning in the nasal cavity," J. Appl. Physiol. **103**, 1082 (2007).
[23]Q. J. Ge, K. Inthavong, and J. Y. Tu, "Local deposition fractions of ultrafine particles in a human nasal-sinus cavity CFD model," Inhalation Toxicol. **24**, 492 (2012).
[24]V. Goodarzi-Ardakani, M. Taeibi-Rahni, M. R. Salimi, and G. Ahmadi, "Computational simulation of temperature and velocity distribution in human upper respiratory airway during inhalation of hot air," Respir. Physiol. Neurobiol. **223**, 49 (2016).
[25]J. Lindemann, H. J. Brambs, T. Keck, K. M. Wiesmiller, G. Rettinger, and D. Pless, "Numerical simulation of intranasal airflow after radical sinus surgery," Am. J. Otolaryngol. **26**, 175 (2005).
[26]I. Hörschler, C. Brücker, W. Schröder, and M. Meinke, "Investigation of the impact of the geometry on the nose flow," Eur. J. Mech.: B/Fluids **25**, 471 (2006).
[27]J. Wen, K. Inthavong, J. Tu, and S. Wang, "Numerical simulations for detailed airflow dynamics in a human nasal cavity," Respir. Physiol. Neurobiol. **161**, 125 (2008).
[28]K. Inthavong, J. Tu, and C. Heschl, "Micron particle deposition in the nasal cavity using the v2-f model," Comput. Fluids **51**, 184 (2011).

Published under license by AIP Publishing

[29]C. Kleinstreuer and Z. Zhang, "Laminar-to-turbulent fluid-particle flows in a human airway model," Int. J. Multiphase Flow **29**, 271 (2003).
[30]J. H. Zhu, H. P. Lee, K. M. Lim, S. J. Lee, L. Teo Li San, and D. Y. Wang, "Inspirational airflow patterns in deviated noses: A numerical study," Comput. Methods Biomech. Biomed. Eng. **16**, 1298 (2013).
[31]J. W. Kim, J. Xi, and X. A. Si, "Dynamic growth and deposition of hygroscopic aerosols in the nasal airway of a 5-year-old child," Int. J. Numer. Methods Biomed. Eng. **29**, 17 (2013).
[32]K. Ito, K. Mitsumune, K. Kuga, N. L. Phuong, K. Tani, and K. Inthavong, "Prediction of convective heat transfer coefficients for the upper respiratory tracts of rat, dog, monkey, and humans," Indoor Built Environ. **26**, 828 (2017).
[33]S. K. Kim, Y. Na, J. I. Kim, and S. K. Chung, "Patient specific CFD models of nasal airflow: Overview of methods and challenges," J. Biomech. **46**, 299 (2013).
[34]T. Wang, D. Chen, P. H. Wang, J. Chen, and J. Deng, "Investigation on the nasal airflow characteristics of anterior nasal cavity stenosis," Braz. J. Med. Biol. Res. **49**, e5182 (2016).
[35]T. Wakayama, M. Suzuki, and T. Tanuma, "Effect of nasal obstruction on continuous positive airway pressure treatment: Computational fluid dynamics analyses," PLoS One **11**, e0150951 (2016).
[36]S. K. Kim, G. E. Heo, A. Seo, Y. Na, and S. K. Chung, "Correlation between nasal airflow characteristics and clinical relevance of nasal septal deviation to nasal airway obstruction," Respir. Physiol. Neurobiol. **192**, 95 (2014).
[37]J. Dong, J. Ma, Y. Shang, K. Inthavong, D. Qiu, J. Tu, and D. Frank-Ito, "Detailed nanoparticle exposure analysis among human nasal cavities with distinct vestibule phenotypes," J. Aerosol Sci. **121**, 54 (2018).
[38]K. Inthavong, P. Das, N. Singh, and J. Sznitman, "In silico approaches to respiratory nasal flows: A review," J. Biomech. **97**, 109434 (2019).
[39]H. Calmet, A. M. Gambaruto, A. J. Bates, M. Vazquez, G. Houzeaux, and D. J. Doorly, "Large-scale CFD simulations of the transitional and turbulent regime for the large human airways during rapid inhalation," Comput. Biol. Med. **69**, 166 (2016).
[40]J. H. Lee, Y. Na, S. K. Kim, and S. K. Chung, "Unsteady flow characteristics through a human nasal airway," Respir. Physiol. Neurobiol. **172**, 136 (2010).
[41]Y. Liu, E. A. Matida, J. Gu, and M. R. Johnson, "Numerical simulation of aerosol deposition in a 3-D human nasal cavity using RANS, RANS/EIM, and LES," J. Aerosol Sci. **38**, 683 (2007).
[42]E. Ghahramani, O. Abouali, H. Emdad, and G. Ahmadi, "Numerical investigation of turbulent airflow and microparticle deposition in a realistic model of human upper airway using LES," Comput. Fluids **157**, 1 (2017).
[43]F. Menter, "Stress-blended eddy simulation (SBES) - A new paradigm in hybrid RANS-LES modeling," Not. Numer. Fluid Mech. Multidiscip. Des. **137**, 27 (2018).
[44]G. J. Brown, D. F. Fletcher, J. W. Leggoe, and D. S. Whyte, "Application of hybrid RANS-LES models to the prediction of flow behaviour in an industrial crystalliser," Appl. Math. Model. **77**, 1797 (2020).
[45]I. Weinhold and G. Mlynski, "Numerical simulation of airflow in the human nose," Eur. Arch. Oto-Rhino-Laryngol. **261**, 452 (2004).
[46]K. Inthavong, Y. Shang, and J. Tu, "Surface mapping for visualization of wall stresses during inhalation in a human nasal cavity," Respir. Physiol. Neurobiol. **190**, 54 (2014).
[47]Y. Shang, J. Dong, K. Inthavong, and J. Tu, "Comparative numerical modeling of inhaled micron-sized particle deposition in human and rat nasal cavities," Inhalation Toxicol. **137**, 27 (2015).
[48]J. Dong, Y. Shang, K. Inthavong, J. Tu, R. Chen, R. Bai, D. Wang, and C. Chen, "Comparative numerical modeling of inhaled nanoparticle deposition in human and rat nasal cavities," Toxicol. Sci. **152**, 284 (2016).
[49]C. Croce, R. Fodil, M. Durand, G. Sbirlea-Apiou, G. Caillibotte, J. F. Papon, J. R. Blondeau, A. Coste, D. Isabey, and B. Louis, "*In vitro* experiments and numerical simulations of airflow in realistic nasal airway geometry," Ann. Biomed. Eng. **34**, 997 (2006).
[50]K. Zhao, P. Dalton, G. C. Yang, and P. W. Scherer, "Numerical modeling of turbulent and laminar airflow and odorant transport during sniffing in the human and rat nose," Chem. Sens. **31**, 107 (2006).
[51]R. A. Segal, G. M. Kepler, and J. S. Kimbell, "Effects of differences in nasal anatomy on airflow distribution: A comparison of four individuals at rest," Ann. Biomed. Eng. **36**, 1870 (2008).
[52]S. Schreck, K. J. Sullivan, C. M. Ho, and H. K. Chang, "Correlations between flow resistance and geometry in a model of the human nose," J. Appl. Physiol. **75**, 1767 (1993).
[53]J. H. Zhu, H. P. Lee, K. M. Lim, S. J. Lee, and D. Y. Wang, "Evaluation and comparison of nasal airway flow patterns among three subjects from caucasian, Chinese and indian ethnic groups using computational fluid dynamics simulation," Respir. Physiol. Neurobiol. **175**, 62–69 (2011).
[54]H. Shi, C. Kleinstreuer, and Z. Zhang, "Laminar airflow and nanoparticle or vapor deposition in a human nasal cavity model," J. Biomech. Eng. **128**, 697 (2006).
[55]J. Bruning, T. Hildebrandt, W. Heppt, N. Schmidt, H. Lamecker, A. Szengel, N. Amiridze, H. Ramm, M. Bindernagel, S. Zachow, and L. Goubergrits, "Characterization of the airflow within an average geometry of the healthy human nasal cavity," Sci. Rep. **10**, 3755 (2020).
[56]E. Sanmiguel-Rojas, M. A. Burgos, C. del Pino, M. A. Sevilla-Garcia, and F. Esteban-Ortega, "Robust nondimensional estimators to assess the nasal airflow in health and disease," Int. J. Numer. Methods Biomed. Eng. **34**, e2906 (2018).
[57]G. J. Garcia, B. M. Hariri, R. G. Patel, and J. S. Rhee, "The relationship between nasal resistance to airflow and the airspace minimal cross-sectional area," J. Biomech. **49**, 1670 (2016).
[58]S. Yu, Y. Liu, X. Sun, and S. Li, "Influence of nasal structure on the distribution of airflow in nasal cavity," Rhinology **46**, 137–143 (2008).
[59]T. Hildebrandt, L. Goubergrits, W. J. Heppt, S. Bessler, and S. Zachow, "Evaluation of the intranasal flow field through computational fluid dynamics," Facial Plast. Surg. **29**, 93 (2013).

Published under license by AIP Publishing